

Spontaneous Magnetization and Nonmagnetic Defect Effects in Mesoscopic $s + is$ Superconductors

G. WANG^a, T.-Y. HAN^a, J. LI^a AND H. HUANG^{b,*}

^a*School of Nuclear Science and Engineering, North China Electric Power University, Beijing 102206, P.R. China*

^b*Department of Mathematics and Physics, North China Electric Power University, Beijing 102206, P.R. China*

Received: 23.09.2024 & Accepted: 27.01.2025

Doi: [10.12693/APhysPolA.147.317](https://doi.org/10.12693/APhysPolA.147.317)

*e-mail: huanghai@ncepu.edu.cn

Based on the two-band time-dependent Ginzburg–Landau theory, we have studied the electromagnetic properties of mesoscopic $s + is$ superconductors with different defect configurations. We have performed our numerical simulations with the finite element method and give direct evidence of spontaneous magnetization induced by the isotropic defect in this superconducting system. Additionally, regarding various impurity numbers, we have investigated the influences of the Ginzburg–Landau parameter κ and defect size on the patterns of spontaneous magnetization distribution. Our theoretical results thus indicate that the defect characteristics will significantly affect the magnetic properties in multiband superconductors with time-reversal symmetry breaking.

topics: time-dependent Ginzburg–Landau theory, finite element method, spontaneous magnetization

1. Introduction

The discovery of the superconducting F-doped LaFeAsO with $T_c \approx 26$ K has caused a boom in the scientific research on iron-based superconductivity [1]. Since then, more than 50 new Fe-based superconductors with similar basic structures have been reported, with the critical temperature reaching up to 56 K [2]. These materials share some general physical properties, and in all known cases, the Fermi surface in the paramagnetic tetragonal phase possesses two concentric hole pockets with dominant d_{xz}/d_{yz} character and two equivalent electron pockets with respectively d_{xz}/d_{xy} and d_{yz}/d_{xy} characters [3]. As the second high-temperature superconductor family, the coexistence of multiband superconductivity and magnetism makes the iron-based compounds of great value in the exploration of the microscopic pairing mechanism and potential applications in spintronics [4–6].

One of the highly interesting problems in iron-based superconductors is the exploration of the possible exotic states with broken time-reversal symmetry (BTRS). For example, as shown by the numerical analysis of the superconducting gap evolution, an intermediate $s + is$ state with the relative phase of order parameters on two hole pockets different from 0 or π will occur in the strongly hole-doped $\text{Ba}_{1-x}\text{K}_x\text{Fe}_2\text{As}_2$ compound [7]. Later on, the reduced $s + is$ Ginzburg–Landau (GL) theory has

been derived from the three-band Eilenberger theory and the interband repulsive interactions relevant to the Fe-based superconductors [8]. Then, the ground state, length scales, and topological excitations have been discussed in detail for this two-band BTRS model. From the perspective of possible experimental detections, Maiti et al. [9] pointed out that the angular dependence of the magnetization distribution is distinct in various BTRS states, and the spontaneous magnetization can be treated as a probe to distinguish different pairing symmetries in the multiband superconductors [9]. Meanwhile, another scheme based on the nonstationary heating process and the thermoelectric effect is also suggested to probe the $s + is$ and $s + id$ superconducting states in candidate iron-based materials [10].

In the present paper, we study the electromagnetic properties of mesoscopic $s + is$ superconductors with the two-band time-dependent Ginzburg–Landau (TDGL) theory. Based on the symmetry consideration of the order parameters, the $s + is$ state with a single isotropic defect is expected to exclude the spontaneous magnetization in the bulk system. With the COMSOL Multiphysics software and the finite element method, we directly demonstrate the existence of spontaneous magnetization induced by the isotropic impurity in this mesoscopic system. Furthermore, we systematically investigate the influence of GL parameter κ and defect radius R on the magnetization distribution for various impurity numbers. Our numerical results indicate that

the defect characteristics will significantly affect the magnetization patterns in the multiband BTRS superconductor.

The paper is organized as follows. In Sect. 2, we introduce the two-band TDGL theory and apply this formalism to the BTRS $s + is$ superconductor. In Sect. 3, we give the procedure of numerical simulations based on the finite element method. Then, in Sect. 4, we discuss the spontaneous magnetization induced by different defect configurations in mesoscopic $s + is$ superconductors. Finally, Sect. 5 gives the conclusion of the paper.

2. Theoretical formalism

The weak-coupling GL free energy functional of a two-gap superconductor can be written as [9–12]

$$F = F_1 + F_2 + F_{12} + \frac{\mathbf{B}^2}{8\pi} \quad (1)$$

with

$$F_i = \frac{1}{2m_i} |\mathbf{\Pi} \Psi_i|^2 - \alpha_i(T) |\Psi_i|^2 + \frac{\beta_i}{2} |\Psi_i|^4 \quad (2)$$

and

$$F_{12} = \gamma_1 |\Psi_1|^2 |\Psi_2|^2 + \frac{\gamma_2}{2} [(\Psi_1^* \Psi_2)^2 + \text{c.c.}] + \frac{1}{2\gamma_3} [(\mathbf{\Pi} \Psi_1)^* \cdot \mathbf{\Pi} \Psi_2 + \text{c.c.}] \quad (3)$$

Here, F_i is the free energy for each band ($i = 1, 2$) and F_{12} is the interaction free energy; Ψ_i represents the superconducting order parameter and m_i is the effective mass for each band; γ_i is the positive phenomenological constant and γ_3 describes the gradient interaction between these two bands. The coefficient α_i is a function of temperature, while β_i is independent of temperature. If the interband interaction is neglected, the functional can be reduced to two independent single-band problems with the corresponding critical temperatures T_{c1} and T_{c2} . Thus, the parameters α_1 and α_2 can be approximately expressed as $\alpha_i(T) = \alpha_{i0} f(\mathbf{r}) t_i(T) = \alpha_{i0} f(\mathbf{r}) (1 - T/T_{ci})$. Here we introduce a function $f(\mathbf{r})$ with +1 or -1 to model the impurity sites, which will deplete the superconducting state at specific positions [13]. We also define the covariant derivative operator $\mathbf{\Pi} = (-i\hbar\nabla - 2e\mathbf{A}/c)$ with the vector potential \mathbf{A} and the magnetic field $\mathbf{B} = \nabla \times \mathbf{A}$.

Typically, the iron pnictides are described by the three-band model, and the three-band superconductivity may exhibit the BTRS $s + is$ state, which will not be present in single- and two-band superconductors. But as shown in [8], the reduced $s + is$ GL functional in (1)–(3) can be derived from the three-band Eilenberger theory and the interband repulsive interactions relevant to the Fe-based superconductors. Moreover, the coefficients of the free energy functional in (1)–(3) obey certain

constraints in the $s + is$ phase. Note that for the energy to be positively defined, the kinetic terms should give the relation $m_1 m_2 - \gamma_3^2 < 0$. Also, for the free energy functional to be bounded from below, the fourth-order terms in the condensates satisfy the constraint $\beta_1 \beta_2 - (\gamma_1 + \gamma_2)^2 > 0$. Furthermore, in the phase where both condensates coexist and the time-reversal symmetry is spontaneously broken, the parameters in the ground state demand the extra conditions $\alpha_{10} \beta_2 - \alpha_{20} (\gamma_1 + \gamma_2) > 0$ and $\alpha_{20} \beta_1 - \alpha_{10} (\gamma_1 + \gamma_2) > 0$.

If the superconductor is driven out of equilibrium, the order parameter should relax back to its equilibrium value. It is well known that this deviation of superconducting materials can be conveniently described by the TDGL theories. The single-band TDGL equations were first proposed by Schmid [14] and derived from the microscopic Bardeen–Cooper–Schrieffer (BCS) theory by Gor’kov and Éliashberg [15]. The extension of TDGL equations to the multi-component superconducting system can be written as [16–18]

$$-I_i \frac{\partial \Psi_i}{\partial t} = \frac{\delta F}{\delta \Psi_i^*} \quad \text{and} \quad -\sigma_n \frac{\partial \mathbf{A}}{\partial t} = \frac{\delta F}{\delta \mathbf{A}}, \quad (4)$$

where I_i is the relaxation time of order parameters and σ_n represents the electrical conductivity of the normal sample in the two-band case. Therefore, minimization of the free energy F with respect to Ψ_i and \mathbf{A} leads to the following dimensionless TDGL equations in the zero-electrostatic potential gauge

$$-I_1 \frac{\partial \Psi_1}{\partial t} = \mathbf{\Pi}^2 \Psi_1 + \frac{m_1}{\gamma_3} \mathbf{\Pi}^2 \Psi_2 - \left[f(\mathbf{r}) t_1(T) - |\Psi_1|^2 - \frac{\gamma_1}{\beta_1} |\Psi_2|^2 \right] \Psi_1 + \frac{\gamma_2}{\beta_1} \Psi_2^2 \Psi_1^*, \quad (5)$$

$$-I_2 \frac{\partial \Psi_2}{\partial t} = \frac{m_1}{m_2} \mathbf{\Pi}^2 \Psi_2 + \frac{m_1}{\gamma_3} \mathbf{\Pi}^2 \Psi_1 - \left[\frac{\alpha_{20}}{\alpha_{10}} f(\mathbf{r}) t_2(T) - \frac{\beta_2}{\beta_1} |\Psi_2|^2 - \frac{\gamma_1}{\beta_1} |\Psi_1|^2 \right] \Psi_2 + \frac{\gamma_2}{\beta_1} \Psi_1^2 \Psi_2^*, \quad (6)$$

and

$$-\frac{\partial \mathbf{A}}{\partial t} = \kappa^2 \nabla \times \nabla \times \mathbf{A} - \mathbf{J}_s \quad (7)$$

with the supercurrent

$$\mathbf{J}_s = \text{Re}(\Psi_1^* \mathbf{\Pi} \Psi_1) + \frac{m_1}{m_2} \text{Re}(\Psi_2^* \mathbf{\Pi} \Psi_2) + \frac{m_1}{\gamma_3} \text{Re}(\Psi_1^* \mathbf{\Pi} \Psi_2 + \Psi_2^* \mathbf{\Pi} \Psi_1). \quad (8)$$

Here, we introduce the coherence length $\xi^2 = \hbar^2 / (2m_1 \alpha_{10})$, the London penetration depth $\lambda^2 = m_1 c^2 / (4\pi e^2 \Psi_0^2)$ with $\Psi_0 = \sqrt{\alpha_{10} / \beta_1}$, and in this case, the GL parameter $\kappa = \lambda / \xi$. The coordinate \mathbf{r} is in units of ξ , the time t is in units of $t_0 = m_1 \sigma_n / (4e^2 \Psi_0^2)$, I_i is in units of $\alpha_{10} t_0$, and the order parameter Ψ is in units of Ψ_0 . We also take the magnetic field \mathbf{B} in units of $B_0 = \Phi_0 / (2\pi \xi^2)$ with the flux quantum $\Phi_0 = \pi \hbar c / e$ and the vector potential \mathbf{A} in units of $A_0 = B_0 \xi$.

In order to numerically solve (5)–(7), we need to specify the appropriate boundary conditions of the superconducting sample. We use the following superconductor–insulator (or vacuum) boundary conditions [19–21]

$$\nabla \Psi_i \cdot \mathbf{n} = 0, \quad \mathbf{A} \cdot \mathbf{n} = 0 \quad \text{and} \quad \nabla \times \mathbf{A} = \mathbf{H}_e, \quad (9)$$

where \mathbf{n} is the outward unit vector normal to the boundary and the external applied magnetic field is set as $\mathbf{H}_e = H_e \hat{\mathbf{z}}$. The first two conditions only indicate that any current passing through the interface between a superconducting domain and vacuum/insulator would be nonphysical. The third equation represents the continuity of the magnetic field across the boundary. The partial differential equations (5)–(7) will be solved numerically for the mesoscopic geometry in the two-dimensional space. The initial conditions at $t = 0$ are taken as $|\Psi_i| = 1$ and $\mathbf{A} = (0, 0)$ on the xy -plane, corresponding to the Meissner state and zero magnetic field inside the superconductor.

3. Finite element method and numerical simulations

Based on the COMSOL Multiphysics software platform [22], we will describe the procedure of the numerical simulations on the TDGL equations in this section. We first split the order parameters into the real and imaginary parts, i.e., $\Psi_1 = u_1 + iu_2$ and $\Psi_2 = u_3 + iu_4$. The magnetic potential is also written in component form as $\mathbf{A} = (u_5, u_6)$. In order to implement the boundary conditions, we introduce an auxiliary variable $u_7(x, y, t)$ for reasons that will be explained below. In the procedure of simulations, we set $\Gamma_1 = 2\Gamma_2 = 1$, $\alpha_{10} = \alpha_{20}$, and $\gamma_1 = 0$. To stabilize the $s + is$ state with a

BTRS phase difference between Ψ_1 and Ψ_2 , we also assume $\beta_1 = \beta_2 = 2\gamma_2$, $m_1 = m_2/2 = \gamma_3/2$ in the calculations.

In this way, we can transform the TDGL equations into the general form of partial differential equations in the COMSOL software package

$$\sum_k \mu_{jk} \frac{\partial u_k}{\partial t} + \sum_l \partial_l \nu_{jl} = \eta_j. \quad (10)$$

Here, we have $j, k = 1, 2, 7$, $l = 1, 2$ and $(\partial_1, \partial_2) = (\partial_x, \partial_y)$. The 7×7 matrix μ_{jk} and the 7×2 column vector ν_{jl} take the form

$$\mu_{jk} = \begin{bmatrix} 1 & 0 & 0 & 0 & 0 & 0 & 0 \\ 0 & 1 & 0 & 0 & 0 & 0 & 0 \\ 0 & 0 & \frac{1}{2} & 0 & 0 & 0 & 0 \\ 0 & 0 & 0 & \frac{1}{2} & 0 & 0 & 0 \\ 0 & 0 & 0 & 0 & 1 & 0 & 0 \\ 0 & 0 & 0 & 0 & 0 & 1 & 0 \\ 0 & 0 & 0 & 0 & 0 & 0 & 0 \end{bmatrix},$$

$$\nu_{jl} = \begin{bmatrix} -u_{1x} - \frac{1}{2}u_{3x} & -u_{1y} - \frac{1}{2}u_{3y} \\ -u_{2x} - \frac{1}{2}u_{4x} & -u_{2y} - \frac{1}{2}u_{4y} \\ -\frac{1}{2}u_{1x} - \frac{1}{2}u_{3x} & -\frac{1}{2}u_{1y} - \frac{1}{2}u_{3y} \\ -\frac{1}{2}u_{2x} - \frac{1}{2}u_{4x} & -\frac{1}{2}u_{2y} - \frac{1}{2}u_{4y} \\ 0 & \kappa^2(u_{6x} - u_{5y} - H_e) \\ \kappa^2(u_{5y} - u_{6x} + H_e) & 0 \\ u_5 & u_6 \end{bmatrix}. \quad (11)$$

Note that the subscript x or y denotes the partial derivative with respect to the corresponding variable here. Meanwhile, the driving force η_j contains all other terms in the TDGL equations except the left-hand side of (10), and detailed calculations will give all the components explicitly as

$$\eta_1 = f(x, y) t_1(T) u_1 - \frac{1}{2} (2u_1^2 + 2u_2^2 + u_3^2 - u_4^2 + 2u_5^2 + 2u_6^2) u_1 + (u_{5x} + u_{6y}) u_2 - \frac{1}{2} (u_5^2 + u_6^2) u_3 + \frac{1}{2} (u_{5x} + u_{6y}) u_4 + (2u_{2x} + u_{4x}) u_5 + (2u_{2y} + u_{4y}) u_6 - u_2 u_3 u_4, \quad (12)$$

$$\eta_2 = f(x, y) t_1(T) u_2 - \frac{1}{2} (2u_1^2 + 2u_2^2 - u_3^2 + u_4^2 + 2u_5^2 + 2u_6^2) u_2 - (u_{5x} + u_{6y}) u_1 - \frac{1}{2} (u_{5x} + u_{6y}) u_3 - \frac{1}{2} (u_5^2 + u_6^2) u_4 - (2u_{1x} + u_{3x}) u_5 - (2u_{1y} + u_{3y}) u_6 - u_1 u_3 u_4, \quad (13)$$

$$\eta_3 = f(x, y) t_2(T) u_3 - \frac{1}{2} (u_1^2 - u_2^2 + 2u_3^2 + 2u_4^2 + u_5^2 + u_6^2) u_3 - \frac{1}{2} (u_5^2 + u_6^2) u_1 + \frac{1}{2} (u_{5x} + u_{6y}) u_2 + \frac{1}{2} (u_{5x} + u_{6y}) u_4 + (u_{2x} + u_{4x}) u_5 + (u_{2y} + u_{4y}) u_6 - u_1 u_2 u_4, \quad (14)$$

$$\eta_4 = f(x, y) t_2(T) u_4 - \frac{1}{2} (u_2^2 - u_1^2 + 2u_3^2 + 2u_4^2 + u_5^2 + u_6^2) u_4 - \frac{1}{2} (u_{5x} + u_{6y}) u_1 - \frac{1}{2} (u_5^2 + u_6^2) u_2 - \frac{1}{2} (u_{5x} + u_{6y}) u_3 - (u_{1x} + u_{3x}) u_5 - (u_{1y} + u_{3y}) u_6 - u_1 u_2 u_3, \quad (15)$$

$$\eta_5 = \frac{1}{2} \left[(2u_{2x} + u_{4x})u_1 - (2u_{1x} + u_{3x})u_2 + (u_{2x} + u_{4x})u_3 - (u_{1x} + u_{3x})u_4 - (2u_1^2 + 2u_2^2 + u_3^2 + u_4^2 + 2u_1u_3 + 2u_2u_4)u_5 \right], \quad (16)$$

$$\eta_6 = \frac{1}{2} \left[(2u_{2y} + u_{4y})u_1 - (2u_{1y} + u_{3y})u_2 + (u_{2y} + u_{4y})u_3 - (u_{1y} + u_{3y})u_4 - (2u_1^2 + 2u_2^2 + u_3^2 + u_4^2 + 2u_1u_3 + 2u_2u_4)u_6 \right], \quad (17)$$

$$\eta_7 = u_{5x} + u_{6y} + u_7. \quad (18)$$

Now, we can examine the boundary conditions in this formalism. With the normal vector $\mathbf{n} = (n_1, n_2)$ and the column vector ν_{jl} , the boundary conditions in (9) can be simply cast into the compact form as

$$\sum_l n_l \nu_{jl} = 0, \quad (19)$$

which is best suited for the COMSOL Multiphysics simulations. We also note that from the equation obtained for ($j = 7$) in (10), our manipulations will give a trivial solution $u_7 = 0$ for this auxiliary variable, ensuring the self-consistency of our formalism.

As a powerful computational tool, COMSOL Multiphysics software can cover a wide range of scientific and engineering fields and employs the finite element method to solve the physical governing equations [23–25]. The starting point for this method is to subdivide the lattice cell into smaller subregions, called elements, which are usually chosen to be quadrilaterals or triangles. The second ingredient in the finite element recipe is to define a space of piecewise polynomial functions with respect to the subdivision of the lattice cell. The two most practical choices are continuous piecewise linear and piecewise quadratic polynomials. The last ingredient, which is crucial for the efficiency of the finite element method, is to choose a set of basis functions that have as small support as possible, i.e., that are nonvanishing over a small subset of the lattice cell. In our problem, we select the triangular mesh elements with a total of 1856 triangle units in the grid division. Secondly, we define a quadratic polynomial function in every subdivision space and choose the Lagrange shape functions as the set of discretized basis functions. Finally, we take the time step $\Delta t = 10^{-2}t_0$ and treat a simulation as converged when the relative variations of the order parameters and the vector potential between two sequential steps are smaller than 10^{-8} .

4. Results and discussions

In this section, we will set the external magnetic field $H_e = 0$ and discuss the corresponding spontaneous magnetization induced by the circular

defects in the mesoscopic $s + is$ superconductor. Following [13], we have chosen the impurity function f to take the phenomenological form

$$f(\mathbf{r}) = \prod_{n=1}^N f_n(\mathbf{r}) \quad (20)$$

with

$$f_n(\mathbf{r}) = \begin{cases} -1 & \text{if } |\mathbf{r} - \mathbf{r}_{0n}| < R, \\ 1 & \text{otherwise.} \end{cases} \quad (21)$$

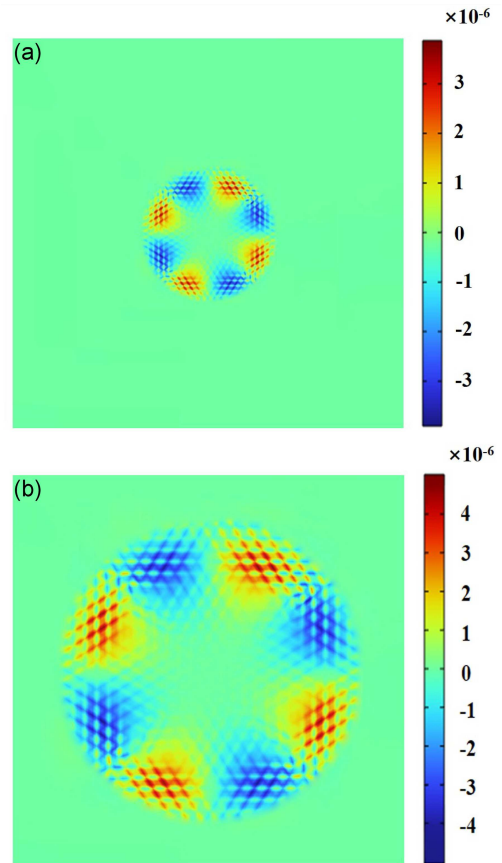


Fig. 1. Spontaneous magnetization induced by a circular defect with the radius (a) $R = 0.2\xi$ or (b) $R = 0.5\xi$ in the $4\xi \times 4\xi$ mesoscopic superconductor. The magnetization only has the component perpendicular to the superconducting plane.

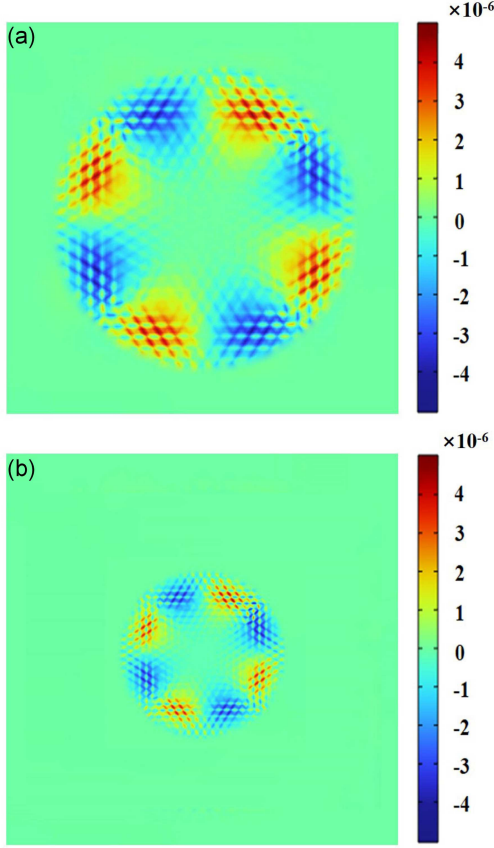


Fig. 2. Spontaneous magnetization induced by a circular defect with the radius $R = 0.5\xi$ in (a) $4\xi \times 4\xi$ or (b) $10\xi \times 10\xi$ mesoscopic superconductor. The magnetization only has the component perpendicular to the superconducting plane.

It is easy to see that the impurities are centered at $\mathbf{r}_{0n} = (x_{0n}, y_{0n})$ with $n = 1, 2, \dots, N$, and the pinning sites are circular with radius R . According to the GL functional in (1)–(3), we can prove that the critical temperature of the multiband superconductor T_c is greater than T_{c1} and T_{c2} . We then set $T_{c1} = 0.9T_c$, $T_{c2} = 0.8T_c$, and $T = 0.7T_c$ in the simulations.

To verify the availability of the method, we first take the impurity number $N = 1$ and insert this pinning site at the center of the superconducting square with a size of $4\xi \times 4\xi$. We also set the GL parameter $\kappa = 1$ and show the snapshots of the spontaneous magnetization $B_z = u_{6x} - u_{5y}$ at $t = 10^3 t_0$ in Fig. 1. In Fig. 1a, we can see that our numerical simulation gives direct evidence of spontaneous magnetization induced by the isotropic defect with $R = 0.2\xi$ in this mesoscopic superconducting system. The maximum spontaneous magnetization B_z^{max} associated with each red (positive) petal is about $3.5 \times 10^{-6} B_0$, while the blue (negative) petals give opposite magnetic field distributions. Furthermore, we observe that the obtained pattern complies with the C_4 rotational symmetry of the square superconducting

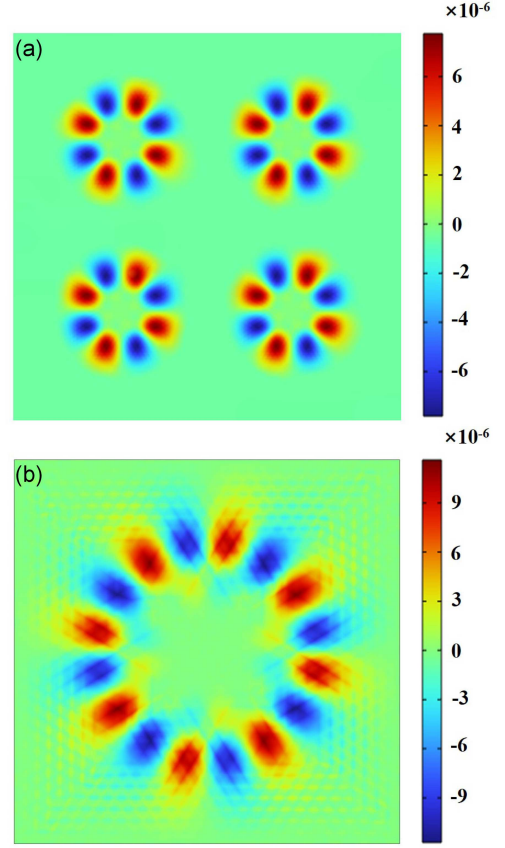


Fig. 3. Spontaneous magnetization induced by (a) four or (b) eight circular defects with the radius $R = 0.2\xi$ in the $4\xi \times 4\xi$ mesoscopic superconductor. The magnetization only has the component perpendicular to the superconducting plane.

sample. With the increase in the defect size to $R = 0.5\xi$, as shown in Fig. 1b, the magnetization distribution extends further away from the pinning center, and the magnetic field is increased to reach a maximum value of $4.5 \times 10^{-6} B_0$.

In this aspect, we also discuss the effect of system size on spontaneous magnetization in the $s + is$ superconductor. We systematically simulate the $4\xi \times 4\xi$ and $10\xi \times 10\xi$ superconducting samples with $\kappa = 1$ and the pinning radius $R = 0.5\xi$. The results are plotted in Fig. 2. It can be seen in Fig. 2 that with the increase in the system size from $4\xi \times 4\xi$ to $10\xi \times 10\xi$, the maximum value of the spontaneous magnetization B_z^{max} decreases from $4.5 \times 10^{-6} B_0$ to $3.8 \times 10^{-6} B_0$. It suggests that the patterns of spontaneous magnetization arise from the combined effects of the central impurity and the sample boundaries.

Furthermore, we also perform simulations on the spontaneous magnetization induced by multiple circular defects in the BTRS mesoscopic superconductors. For $N = 4$ and $\kappa = 1$, we select the impurity sites at $(\pm\xi, \pm\xi)$ and plot the spontaneous magnetization at $t = 10^3 t_0$ in Fig. 3a.

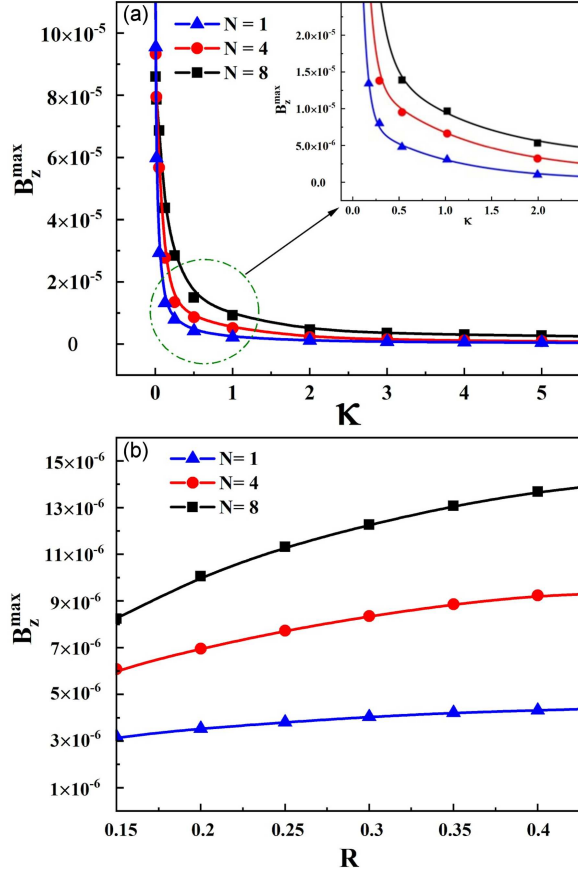


Fig. 4. Variation of the maximum spontaneous magnetization with (a) the GL parameter κ or (b) the defect radius R for different impurity numbers in the $4\xi \times 4\xi$ mesoscopic superconductor.

We observe that B_z generated around each pinning position exhibits the identical configuration and its maximum value at red or blue petal is $7.0 \times 10^{-6} B_0$. For $N = 8$, we take the pinning sites at $(\pm 1.2\xi, \pm 0.5\xi)$ and $(\pm 0.5\xi, \pm 1.2\xi)$, respectively, and plot the spontaneous magnetization in Fig. 3b. In Fig. 3b, it is shown that with the increase in the impurity number, we can obtain different patterns of spontaneous magnetization distribution and B_z^{\max} raises to about $1.0 \times 10^{-5} B_0$ under such conditions.

Meanwhile, we also calculate the maximum spontaneous magnetization as a function of the GL parameter κ and the defect radius R for the impurity number $N = 1, 4, 8$, as mentioned above. It can be seen in Fig. 4a that for $R = 0.2\xi$, B_z^{\max} decreases sharply as κ increases, and then the three curves converge to the value of zero when κ is sufficiently large. We observe that similar to the single-band case [26], a larger GL parameter κ generally produces a stronger superconducting order parameter or a weaker spontaneous magnetization intensity. Our numerical data also indicate that within a relatively broad range of κ , a larger number of

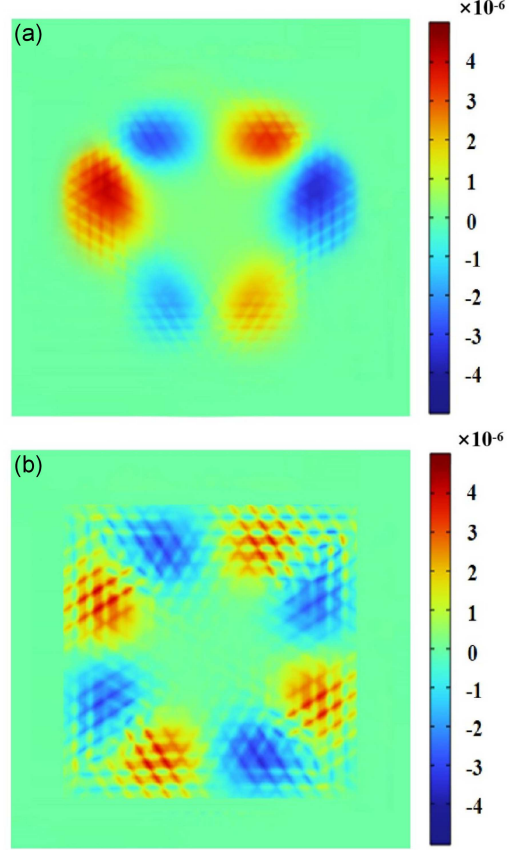


Fig. 5. Spontaneous magnetization induced by (a) triangular or (b) quadrilateral defect in the $4\xi \times 4\xi$ mesoscopic superconductor. The magnetization only has the component perpendicular to the superconducting plane.

defects always results in greater B_z^{\max} . Figure 4b shows the spontaneous magnetization with respect to the defect radius R for $\kappa = 1$. It is easy to see that B_z^{\max} grows with the increase in R , and this trend becomes more apparent for a higher defect number due to the decrease in the effective superconducting area of the material.

For a typical single-band superconductor, the GL parameter κ is an effective phenomenological parameter that can be used to distinguish between type-I and type-II superconductors. When we cross the boundary at $\kappa = 1/\sqrt{2}$, it may induce a transition from the Meissner state to the Abrikosov vortex phase in the external magnetic field, and therefore, a dramatic change in magnetic behaviors in the superconductor. However, we study the impurity-induced spontaneous magnetization in the multiband superconducting system here. The supercurrent and local spontaneous magnetization are generated by the BTRS $s + is$ state. In the whole range of κ , the superconductor will remain in this state with the algebraic sum of the magnetic field strength B_z in the entire mesoscopic sample equal to zero. Since neither an applied magnetic field nor

a phase transition exists in this process, the B_z^{\max} will not show an abrupt variation in this BTRS system.

At this point, we would also like to discuss the effect of triangular and quadrilateral defect configurations on spontaneous magnetization. Both of these impurities have a side length of ξ and are placed at the center of $4\xi \times 4\xi$ mesoscopic superconducting systems. We select the vertex coordinates of the triangular impurity at $(\pm 0.5\xi, \sqrt{3}\xi/6)$ and $(0, -\sqrt{3}\xi/3)$, and the quadrilateral ones at $(\pm 0.5\xi, \pm 0.5\xi)$. We also take the impurity function $f(\mathbf{r}) = -1$ inside the defects and $f(\mathbf{r}) = 1$ otherwise. The numerical results with the GL parameter $\kappa = 1$ are plotted at $t = 10^3 t_0$ in Fig. 5. It can be seen from Fig. 5 that the maximum values of the spontaneous magnetization B_z^{\max} are $4.2 \times 10^{-6} B_0$ and $4.6 \times 10^{-6} B_0$ for the triangular and quadrilateral defects, respectively. For the triangular impurity, we observe the magnetic petals with different sizes, while in the quadrilateral case, the C_4 symmetry is still preserved and the magnetic distribution is similar to the circular one.

5. Conclusions

Based on the two-band TDGL theory, we have investigated the electromagnetic characteristics of mesoscopic $s + is$ superconductors with different defect configurations. We have performed the numerical simulations with the finite element method and given direct evidence of spontaneous magnetization induced by the isotropic defect in this superconducting system. We have also explored the impacts of GL parameter κ and defect size on the spontaneous magnetization distribution within this multiband BTRS superconductor. Our theoretical results demonstrate that boundary current effects can arise in the superconducting states that are neither topological nor chiral according to the modern classification.

References

- [1] Y. Kamihara, T. Watanabe, M. Hirano, H. Hosono, *J. Am. Chem. Soc.* **130**, 3296 (2008).
- [2] C. Wang, L.J. Li, S. Chi et al., *Europhys. Lett.* **83**, 67006 (2008).
- [3] O.K. Andersen, L. Boeri, *Ann. Phys.* **523**, 8 (2011).
- [4] I.I. Mazin, D.J. Singh, M.D. Johannes, M.H. Du, *Phys. Rev. Lett.* **101**, 057003 (2008).
- [5] K. Kuroki, S. Onari, R. Arita, H. Usui, Y. Tanaka, H. Kontani, H. Aoki, *Phys. Rev. Lett.* **101**, 087004 (2008).
- [6] A.V. Chubukov, D.V. Efremov, I. Eremin, *Phys. Rev. B* **78**, 134512 (2008).
- [7] S. Maiti, A.V. Chubukov, *Phys. Rev. B* **87**, 144511 (2013).
- [8] J. Garaud, M. Silaev, E. Babaev, *Physica C* **533**, 63 (2017).
- [9] S. Maiti, M. Sigrist, A. Chubukov, *Phys. Rev. B* **91**, 161102(R) (2015).
- [10] J. Garaud, M. Silaev, E. Babaev, *Phys. Rev. Lett.* **116**, 097002 (2016).
- [11] V.L. Vadimov, M.A. Silaev, *Phys. Rev. B* **98**, 104504 (2018).
- [12] W.C. Goncalves, E. Sardella, V.F. Becerra, M.V. Milošević, F.M. Peeters, *J. Math. Phys.* **55**, 041501 (2014).
- [13] M.P. Sørensen, N.F. Pedersen, M. Ögren, *Physica C* **533**, 40 (2017).
- [14] A. Schmid, *Phys. Kondens. Mater.* **5**, 302 (1966).
- [15] L.P. Gor'kov, G.M. Éliashberg, *Zh. Eksp. Teor. Fiz.* **54**, 612 (1968).
- [16] P.A.S. Mosquera, R.M. da Silva, A. Vagov, A.A. Shanenko, T.C.E. Deluque, A.J. Albino, *Phys. Rev. B* **96**, 054517 (2017).
- [17] C.A. Aguirre, M.R. Joya, J. Barba-Ortega, *Physica C* **585**, 1353867 (2021).
- [18] S.Z. Du, Y.N. Zhong, S.W. Yao, L. Peng, T.T. Shi, L.N. Sang, X.L. Liu, J. Lin, *Phys. Lett. A* **443**, 128206 (2022).
- [19] S.W. Yao, L. Peng, J. Lin, J. Chen, C.B. Cai, Y. Zhou, *J. Low. Temp. Phys.* **202**, 329 (2021).
- [20] Y.G. Ryu, G.I. Mun, Y.N. Kwon, S.H. Kim, S. Hong, *Physica C* **602**, 1354125 (2022).
- [21] Y.G. Ryu, J.H. Om, J.H. Kim, G.I. Ro, G.I. Mun, S. Hong, *J. Supercond. Nov. Magn.* **37**, 527 (2024).
- [22] COMSOL, *Multiphysics Reference Manual*, 2019.
- [23] Q. Du, M.D. Gunzburger, J.S. Peterson, *Phys. Rev. B* **46**, 9027 (1992).
- [24] T.S. Alstrøm, M.P. Sørensen, N.F. Pedersen, S. Madsen, *Acta Appl. Math.* **115**, 63 (2011).
- [25] B. Oripov, S.M. Anlage, *Phys. Rev. E* **101**, 033306 (2020).
- [26] Y. Zhao, J. Xi, *Supercond. Nov. Magn.* **36**, 1343 (2023).